UC Davis
UC Davis Previously Published Works

Title

PET Image Reconstruction Using Kernel Method

Permalink

Journal

ISSN

Authors

Wang, Guobao
Qi, Jinyi

Publication Date

2015

DOI

PET Image Reconstruction Using Kernel Method

Guobao Wang [Senior Member, IEEE] and **Jinyi Qi [Fellow, IEEE]**
Department of Biomedical Engineering, University of California, Davis, CA 95616, USA

Guobao Wang: gbwang@ucdavis.edu; Jinyi Qi: qi@ucdavis.edu

Abstract

Image reconstruction from low-count PET projection data is challenging because the inverse problem is ill-posed. Prior information can be used to improve image quality. Inspired by the kernel methods in machine learning, this paper proposes a kernel based method that models PET image intensity in each pixel as a function of a set of features obtained from prior information. The kernel-based image model is incorporated into the forward model of PET projection data and the coefficients can be readily estimated by the maximum likelihood (ML) or penalized likelihood image reconstruction. A kernelized expectation-maximization (EM) algorithm is presented to obtain the ML estimate. Computer simulations show that the proposed approach can achieve better bias versus variance trade-off and higher contrast recovery for dynamic PET image reconstruction than the conventional maximum likelihood method with and without post-reconstruction denoising. Compared with other regularization-based methods, the kernel method is easier to implement and provides better image quality for low-count data. Application of the proposed kernel method to a 4D dynamic PET patient dataset showed promising results.

Index Terms

PET; image reconstruction; image prior; kernel method; expectation maximization

I. Introduction

Positron emission tomography (PET) can image biochemical processes *in vivo* using radioactive tracers. To monitor rapid change in tracer distribution, short scan durations must be used, which often results in low counting statistics (i.e., high noise). Image reconstruction from low-count PET projection data is challenging because the inverse problem is ill-posed and the resultant image is usually very noisy. To improve the quality of reconstructed images, it is desirable to incorporate prior information in PET image reconstruction [1]. Such information can be obtained either from a composite time frame of a dynamic PET scan that has a longer scan duration, or from a co-registered anatomical image that has good tissue contrasts[1].

---

[1]The term "prior" used here refers to any information that is obtained before image reconstruction and may not follow the strict statistical definition.

A common way to incorporate prior knowledge in PET image reconstruction is through the use of edge-preserving regularization. A recent review on using anatomical prior information for PET image reconstruction can be found in [2]. Among different regularization methods [3]–[8], [10]–[13], the Bowsher method [9], which adaptively chooses neighboring pixels for each pixel in the image estimate using information from a prior image, was found to utilize anatomical prior information better than others in terms of performance and computational complexity [16]. The nonlocal regularization [17] can incorporate anatomical weights through a methodology similar to the neighborhood selection in the Bowsher method [14], [15] to improve emission reconstruction [18]–[20]. Alternatively, the prior image constrained compressive sensing (PICCS, [21]–[23]), an iterative reconstruction approach introduced in the context of dynamic computed tomography (CT), explores sparsity on the difference image between the image estimate and a composite image. PICCS can be adapted for use in PET image reconstruction [24].

Besides the regularized image reconstruction methods, post-reconstruction denoising methods can also incorporate prior information to improve PET image quality [20], [27], [31], [32]. The highly constrained back-projection (HYPR, [25], [26]), which was originally developed in magnetic resonance imaging (MRI) for image reconstruction from under-sampled data, is a method of using a composite image prior and has been applied to denoising dynamic PET images [27]. Nonlocal means (NLM, [30]) is another method that incorporates prior knowledge into image denoising [20], [31]. Post-reconstruction denoising is usually easier to implement than regularization-based reconstruction methods.

In this paper, we propose a new way to incorporate image derived prior information in PET image reconstruction. We directly model the PET image intensity at pixel j, x_j, as a function Γ of a set of features, f_j, which is derived from available prior information at pixel j. The function $x_j = \Gamma(f_j)$ can be very complex. Inspired by the kernel methods in machine learning [28], we model the complex function $\Gamma(f_j)$ as a linear function in a higher-dimensional transformed space of $\{f_j\}$ that is implicitly determined by a kernel function. The kernelized image model can then be incorporated into the forward projection model of PET to perform maximum likelihood (ML) image reconstruction without an explicit regularization function. The expectation-maximization (EM) [33], [34] algorithm with and without ordered subsets [35] can be directly applied to obtain the ML estimate.

The proposed kernelized EM method has the same simplicity as the conventional ML EM reconstruction followed by post-reconstruction denoising. We expect the former method to result in better performance than the latter for low-count data because it models noise in the projection domain where PET data are well modeled by independent Poisson random variables. The latter method requires a noise model in the image domain where noise is highly correlated and the covariance matrix is very difficult to estimate. The benefit of modeling noise in the projection domain over that in the image domain can become significant when the count level of PET data is low. Compared to regularization-based methods, the advantage of the proposed kernel-based EM reconstruction is its simplicity in implementation and readiness to be merged into the OSEM algorithm that is already available in commercial clinical PET scanners.

Part of this work was presented at the 2013 IEEE International Symposium on Biomedical Imaging [36]. Zhou *et al* also presented a kernel-based method for compressive sensing (CS) dynamic MRI image reconstruction at the same conference [37]. Both methods share the same spirit of using the kernel trick but the technical aims are different. The kernel-based CS [37], [38] employs *explicit* mapping functions, such as kernel principal components or polynomial functions, to transform the projection data into a higher dimensional feature space where the projection data are nonlinearly sparse. A reverse estimation is required to convert the reconstructed coefficients back to the original image. In comparison, this paper uses an *implicit* mapping function through kernels to model PET image intensity as a linear function in the kernel space determined by prior images. Our work provides a novel method of using prior image information for improving image reconstruction.

This paper is organized as follows. We start with a brief description of PET image reconstruction in Section II and then describe the kernel model for image representation and kernel-based PET image reconstruction. Section III presents computer simulation studies comparing the kernel method with other regularization methods. An application of the proposed method to a dynamic PET patient data set is given in Section V. Finally conclusions are drawn in Section VI.

II. Theory

A. PET Image Reconstruction

PET projection data $\boldsymbol{y}$ are well modeled as independent Poisson random variables with the log-likelihood function [1]

$$L(\boldsymbol{y}|\boldsymbol{x}) = \sum_{i=1}^{M} y_i \log \overline{y}_i - \overline{y}_i - \log y_i! \quad (1)$$

where M is the total number of lines of response and the expectation $\bar{\boldsymbol{y}}$ is related to the unknown emission image $\boldsymbol{x}$ through

$$\overline{\boldsymbol{y}} = \boldsymbol{P}\boldsymbol{x} + \boldsymbol{r} \quad (2)$$

with $\boldsymbol{P}$ being the detection probability matrix and $\boldsymbol{r}$ the expectation of random and scattered events.

The maximum likelihood (ML) estimate of the image $\boldsymbol{x}$ is found by maximizing the Poisson log likelihood

$$\hat{\boldsymbol{x}} = \arg\max_{\boldsymbol{x} \geq \boldsymbol{0}} L(\boldsymbol{y}|\boldsymbol{x}). \quad (3)$$

The expectation-maximization (EM) algorithm [33] is derived to find the solution by the following iterative update

$$x^{n+1} = \frac{x^n}{P^T 1_M} \cdot \left(P^T \frac{y}{Px^n + r} \right), \quad (4)$$

where 1_M is a vector of length M with all elements being 1, n denotes iteration number and the superscript "T" denotes matrix transpose. The vector multiplication and division are element-wise operations.

While the ML estimate can be very noisy at convergence, penalized likelihood (PL) methods seek an image estimate by maximizing the penalized Poisson log likelihood

$$\hat{x} = \arg \max_{x \geq 0} L(y|x) - \beta U(x), \quad (5)$$

where β is a hyperparameter that controls the strength of the regularization and $U(x)$ is an image roughness penalty that can take the following anisotropic form

$$U(x) = \sum_{j=1}^{N} \sum_{k \in \mathcal{N}_j} w_{jk} \psi_\delta(x_j - x_k), \quad (6)$$

where the weighting factor w_{jk} is inversely proportional to the distance between pixel j and pixel k in the neighborhood $\mathcal{N}_j$. The second order neighborhood is usually used that consists of 8 nearest pixels in 2D and 26 nearest voxels in 3D. $\psi_\delta(t)$ is the penalty function, e.g. $\psi_\delta(t) = \sqrt{t^2 + \delta^2}$, and δ is a parameter that controls the smoothness of the penalty function. N is the total number of pixels in the image. $U(x)$ can also take the isotropic total variation (iTV) form

$$U(x) = \sum_{j=1}^{N} \psi_\delta \left(\sqrt{\sum_{k \in \mathcal{N}_j} w_{jk}(x_j - x_k)^2} \right). \quad (7)$$

Information from a prior image can be incorporated in $U(x)$. For example, the Bowsher method and nonlocal regularization approach set the weighting factor w_{jk} in each neighborhood adaptively based on a prior image [7], [17]. PICCS includes a regularization on the difference image between x and a prior image, instead of regularizing x itself [21]. Compared to the EM update equation (4) for ML reconstruction, optimization algorithms for PL reconstruction (5) are more complicated, depending on the complexity of the regularization function $U(x)$.

B. Image Representation by Kernels

Inspired by the kernel machines in machine learning [28], we propose a kernel based image representation for PET images.

We first identify a set of low-dimensional features f_j for each pixel j. The "label" value for f_j is the image intensity value at j, denoted as x_j, and can be described as a function of f_j by

$$x_j = \Gamma(\boldsymbol{f}_j). \quad (8)$$

A linear form $\Gamma(\boldsymbol{f}) = \boldsymbol{w}^T\boldsymbol{f}$ is the simplest model but may represent image intensity poorly when $\Gamma(\boldsymbol{f})$ is actually nonlinear and complex.

While $\Gamma(\boldsymbol{f})$ cannot be accurately described as linear in the low-dimensional space spanned by $\{\boldsymbol{f}_j\}_{j=1}^N$, it is possible to describe $\Gamma(\boldsymbol{f})$ linearly in a transformed space $\{\phi(\boldsymbol{f}_j)\}_{j=1}^N$ of very-high dimension,

$$\Gamma(\boldsymbol{f}_j) = \boldsymbol{w}^T\phi(\boldsymbol{f}_j), \quad (9)$$

where $\phi(\boldsymbol{f})$ is a mapping function and $\boldsymbol{w}$ is a weight vector which also sits in the transformed space:

$$\boldsymbol{w} = \sum_{l=1}^N \alpha_l \phi(\boldsymbol{f}_l) \quad (10)$$

with $\boldsymbol{\alpha}$ being the coefficient vector. By substituting (10) into (9), the kernel representation for the image intensity at pixel j is written as

$$x_j = \sum_{l=1}^N \alpha_l \phi(\boldsymbol{f}_l)^T \phi(\boldsymbol{f}_j) = \sum_{l=1}^N \alpha_l \kappa(\boldsymbol{f}_j, \boldsymbol{f}_l), \quad (11)$$

where $\kappa(\boldsymbol{f}_j, \boldsymbol{f}_l) \triangleq \phi(\boldsymbol{f}_l)^T \phi(\boldsymbol{f}_j)$ is a kernel[2]. The equivalent matrix-vector form of (11) is

$$\boldsymbol{x} = \boldsymbol{K}\boldsymbol{\alpha}, \quad (12)$$

where the (j, l)th element of the kernel matrix $\boldsymbol{K}$ is $\kappa(\boldsymbol{f}_j, \boldsymbol{f}_l)$. In (12), each column of $\boldsymbol{K}$ can be considered as a basis function for image representation.

The image intensity x_j at pixel j is thus a linear function in the kernel space but is nonlinear in the original space of feature points $\{\boldsymbol{f}_j\}_{j=1}^N$. Note that the mapping function ϕ is implicitly defined by the kernel $\kappa(\cdot, \cdot)$ and is not required to be known. Typical kernels include the radial Gaussian kernel

$$\kappa(\boldsymbol{f}_j, \boldsymbol{f}_l) = \exp\left(-\frac{\|\boldsymbol{f}_j - \boldsymbol{f}_l\|^2}{2\sigma^2}\right), \quad (13)$$

which has a mapping function ϕ of infinite dimension [28], and the polynomial kernel

---

[2]Note that the kernel defined here should not be confused with image basis functions, which sometime are also called "kernels".

$$\kappa(\boldsymbol{f}_j, \boldsymbol{f}_l) = \left(\boldsymbol{f}_j^T \boldsymbol{f}_l + c\right)^d. \quad (14)$$

σ, c and d are the kernel parameters in the respective kernels. The polynomial kernel reduces to the linear kernel when $d = 1$.

C. Kernel Method for Image Reconstruction

Substituting the kernel-based image model (12) into the PET forward model (2), we obtain the following kernel based forward projection model:

$$\overline{\boldsymbol{y}} = \boldsymbol{P}\boldsymbol{K}\boldsymbol{\alpha} + \boldsymbol{r}. \quad (15)$$

The forward model in (2) is a special case of the kernelized model (15) with

$$\boldsymbol{K} = \boldsymbol{I}, \quad (16)$$

where $\boldsymbol{I}$ denotes the identity matrix. The advantage of (15) is that prior knowledge from other resources (e.g. whole dynamic frames in dynamic PET, or multi-modality images) can be incorporated into the forward projection model, which consequently improves the reconstruction of the low-count scan.

Combining the kernel based projection model (15) and the Poisson likelihood function (1), the kernel coefficient image $\boldsymbol{\alpha}$ can be estimated by

$$\hat{\boldsymbol{\alpha}} = \arg\max_{\boldsymbol{\alpha} \geq \boldsymbol{0}} L(\boldsymbol{y}|\boldsymbol{K}\boldsymbol{\alpha}) - \beta V(\boldsymbol{\alpha}), \quad (17)$$

where $V(\boldsymbol{\alpha})$ is an optional penalty function and β is the regularization parameter. Once the coefficient image $\boldsymbol{\alpha}$ is estimated, the reconstructed emission image is calculated by

$$\hat{\boldsymbol{x}} = \boldsymbol{K}\hat{\boldsymbol{\alpha}}. \quad (18)$$

Because the reconstructed image is already regularized by the kernels, we set $\beta = 0$ in this work to obtain the maximum likelihood estimate of $\boldsymbol{\alpha}$ by

$$\hat{\boldsymbol{\alpha}} = \arg\max_{\boldsymbol{\alpha} \geq \boldsymbol{0}} L(\boldsymbol{y}|\boldsymbol{K}\boldsymbol{\alpha}). \quad (19)$$

The standard ML EM algorithm [33] given in Eq. (4) can be directly applied to find the ML estimate of $\boldsymbol{\alpha}$ because (15) is in a linear form and $\boldsymbol{PK}$ can be treated as single matrix. The resulting kernelized EM update of $\boldsymbol{\alpha}$ at iteration $(n + 1)$ is

$$\boldsymbol{\alpha}^{n+1} = \frac{\boldsymbol{\alpha}^n}{\boldsymbol{K}^T \boldsymbol{P}^T \boldsymbol{1}_M} \cdot \left(\boldsymbol{K}^T \boldsymbol{P}^T \frac{\boldsymbol{y}}{\boldsymbol{P}\boldsymbol{K}\boldsymbol{\alpha}^n + \boldsymbol{r}}\right). \quad (20)$$

Alternatively, one can decouple P and K using the nested EM algorithm [39].

Compared with using an edge-preserving penalty function to incorporate prior information, the above kernel-based ML EM algorithm is easier to implement.

D. Practical Construction of Kernel Matrix

A full kernel matrix K of an image is usually too large to be used in practice. We adopt the k-nearest neighbors (kNN, [29]) that is widely used for graph construction in machine learning to construct a sparse matrix. The kNN method finds k similar neighbors for each pixel and defines the (j, l)th element of the kernel matrix K by

$$K_{jl} = \begin{cases} \kappa(\boldsymbol{f}_j, \boldsymbol{f}_l), & \boldsymbol{f}_l \in k\text{NN of } \boldsymbol{f}_j, \\ 0, & \text{otherwise.} \end{cases} \quad (21)$$

where kNN is sought based on the Euclidean distance between $\boldsymbol{f}_j$ and $\boldsymbol{f}_l$. Since a constant-k neighboring pixels are used, this above method may oversmooth a small target that has far less than k actual neighbors. An alternative to kNN is the ε-ball method, which assigns 0 to the neighbors that are outside the ε-ball of a pixel:

$$K_{jl} = \begin{cases} \kappa(\boldsymbol{f}_j, \boldsymbol{f}_l), & \text{dist}(\boldsymbol{f}_j, \boldsymbol{f}_l) \leq \varepsilon, \\ 0, & \text{otherwise.} \end{cases} \quad (22)$$

Each pixel thus can find an adaptive number of neighbors.

The computation cost of the kNN and ε-ball method can be expensive when the total number of pixels, N, is large. Alternatively, the kernel matrix can be defined only using a local neighborhood by

$$K_{jl} = \begin{cases} \kappa(\boldsymbol{f}_j, \boldsymbol{f}_l), & l \in \mathcal{N}_j, \\ 0, & \text{otherwise.} \end{cases} \quad (23)$$

where $\mathcal{N}_j$ denotes the neighborhood of pixel j. These three strategies stated above can be combined to improve the robustness of the kernel method as we will demonstrate later.

The feature set $\{\boldsymbol{f}_j\}_{j=1}^N$ is required for constructing the kernel matrix. A general requirement is that the feature set should be large enough so that the PET image intensity can be determined uniquely by the features. For data acquired on a multi-modality scanner, such as PET/CT or PET/MR, the features can be obtained from co-registered anatomical images. For dynamic PET data, the feature vector $\boldsymbol{f}_j$ associated with a pixel j can be derived from an initial reconstruction of later frames or of the summed sinogram of different time frames.

In order to make it easy to choose a kernel parameter (e.g. σ in the Gaussian kernel), the feature points $\{\boldsymbol{f}_j\}$ can be first normalized by its standard derivation using

$$\overline{f}_{j,m} = \frac{f_{j,m}}{\sigma_m(\boldsymbol{f})} \quad (24)$$

where $\sigma_m(\boldsymbol{f})$ is the standard deviation of the mth element of $\boldsymbol{f}_j$ over all of the pixels.

Instead of $\boldsymbol{K}$, the normalized matrix $\overline{\boldsymbol{K}}$,

$$\overline{\boldsymbol{K}} = \mathrm{diag}^{-1}[\boldsymbol{K}\boldsymbol{1}_N]\boldsymbol{K}, \quad (25)$$

can be used. We found $\overline{\boldsymbol{K}}$ resulted in higher image quality than $\boldsymbol{K}$ in our simulation.

While the use of a kernel matrix in the kernel method requires extra memory and computation, the kernel matrix is very sparse so the extra memory and computation cost are relatively small compared with the large size of the system matrix and computation time of forward and back projections. In our simulation and real data studies, we observed that the additional computation cost of the kernel matrix was only 10% of the total image reconstruction time.

III. Simulation Studies

The proposed kernel method applies spatial-adaptive smoothing based on prior images and has applications in both anatomical-prior guided PET image reconstruction and dynamic PET reconstruction. Here we apply the method to frame-by-frame image reconstruction of dynamic PET data.

A. Dynamic PET Simulation Setup

Dynamic PET scans were simulated for a GE DST whole-body PET scanner using a Zubal head phantom (Fig. 1(a)). The scanning schedule consisted of 24 time frames: 4×20 s, 4×40 s, 4×60 s, 4×180 s and 8×300 s. Regional time activity curves shown in Fig. 1(b) were assigned to different brain regions. Dynamic activity images were first forward projected to generate noise-free sinograms. Poisson noise was then introduced. Scatters were simulated using the SimSET package [52]. We also included 20% uniform random events. Attenuation map, mean scatters and randoms were used in all reconstruction methods to obtain quantitative images. The expected total number of events over 60 minutes was 8 million. Ten noisy realizations were simulated and each was reconstructed independently for comparison.

We compared the proposed kernelized EM (KEM) algorithm with the conventional ML-EM reconstruction [34], PL reconstruction using total variation (TV) regularization [40], ML-EM followed by post-reconstruction denoising methods (HYPR [27] and NLM [30]), PL reconstruction using the Bowsher method [9] and PICCS [21] to incorporate the image prior. All regularization-based methods used the De Pierro's EM algorithm [41] with 200 iterations. All the aforementioned methods, except the ML-EM, make use of spatial smoothing to improve image quality. We note that temporal regularization methods have also been developed to improve dynamic image reconstruction, such as the temporal

filtering methods [42]–[45] and reconstruction using smooth temporal basis functions [46], [47]. Readers are referred to [48]–[50] for detailed reviews on the development of temporal smoothing techniques. Two temporal-based methods were included here for comparisons. The first one is the EM reconstruction followed by a temporal filtering based on the principal component analysis (PCA) [43]. The second method is the penalized weighted least squares reconstruction in the Karhunen-Loeve (KL) transform domain (KL-PWLS) developed by Wernick *et al* [46], which essentially models the dynamic sinogram in the KL transform domain and reconstructs each coefficient image separately from the corresponding transformed sinogram. These two PCA-based methods share similar simplicity as the proposed kernel method.

B. Use of Composite Images

To construct the kernel matrix, we propose to obtain the prior images from composite frames in dynamic PET. Multiple short time frames are summed together to improve the counting statistics and reduce noise. Although temporal information is lost, common spatial information shared by different time frames is well preserved in the summed frames and can be used to aid the reconstruction of short time frames. Choosing a proper number of composite frames is important for reconstructing high-quality images. On one hand, a small number of composite frames reduces noise in composite images, but is at the risk of losing important spatial information in the kernel matrix. On the other hand, a large number of composite frames can preserve spatial information but may be ineffective in suppressing noise. We found that using three composite frames provided a good balance between preserving spatial information and reducing noise in the composite images.

The rebinned sinograms $\{ \boldsymbol{y}_m^{\text{reb}} \}_{m=1}^3$, each with 20 minutes, were reconstructed using the conventional ML EM algorithm with 100 iterations. The reconstructed images $\{ \hat{\boldsymbol{x}}_m^{\text{reb}} \}_{m=1}^3$ of the three rebinned frames, shown in Fig. 2, were used as the prior images in all spatial smoothing reconstruction methods, except the ML-EM and PL with TV regularization, which do not use any composite image prior information from dynamic data.

For the proposed KEM method, the reconstructed activities of the three rebinned frames were used to form the feature points $\{ \boldsymbol{f}_j \}_{j=1}^N$,

$$\boldsymbol{f}_j = [\hat{x}_{j,1}^{\text{reb}}, \hat{x}_{j,2}^{\text{reb}}, \hat{x}_{j,3}^{\text{reb}}]^T \quad (26)$$

where $\hat{x}_{j,m}^{\text{reb}}$ is the image intensity value at pixel j in the rebinned time frame m, $m = 1, 2, 3$. $k = 48$ nearest neighbors of each $\boldsymbol{f}_j$ were then sought by knnsearch in MATLAB using the scaled Euclidean distance. A sparse kernel matrix $\boldsymbol{K}$ was then calculated using $\{ \boldsymbol{f}_j \}$ by Eq. (21). We used the radial Gaussian kernel (13) with $\sigma = 1$.

Each column j of $\boldsymbol{K}$ can be seen as a basis image function with a_j the corresponding basis coefficient. Fig. 3 shows the basis images obtained by reshaping the columns of $\boldsymbol{K}$ that correspond to the locations "A", "B", "C" and "D" indicated in Fig. 1(a). These four pixels are located in the blood region, the gray matter boundary, the white matter and the tumor

region, respectively. The basis images are sparse and self-adapt to the corresponding pixel locations.

The same kernel matrix $\bar{K}$ employed in KEM was also used as the weighting matrix in the NLM denoising method [30]. The HYPR method [27] used the sum of the three rebinned images as the composite image and a 7×7 window for Gaussian smoothing. In the PICCS method [21], the three prior images were used as the reference image for the individual frames in the early, middle and late 20 minutes, respectively. TV regularization [40] was used in PICCS with the parameter α that balances spatial smoothness and prior image constraint set to 0.7. The Bowsher method [9] used a quadratic penalty function and used the radial Gaussian distance of $\{f_j\}$ in (13) to choose pixels in the local neighborhoods. The neighborhood size in the Bowsher method was set to 7×7 and 20 pixels were selected for each neighborhood. These parameters in different methods were chosen to minimize the image MSE.

C. Comparison of Different Reconstruction Methods

For quantitative comparison between different reconstruction methods, we computed the ensemble mean squared bias, variance, and mean squared error (MSE), which are defined by

$$\text{Bias}^2 = \sum_{j=1}^{N}(\overline{x}_j - x_j^{\text{true}})^2 / \sum_{j=1}^{N}(x_j^{\text{true}})^2, \quad (27)$$

$$\text{Var} = \frac{1}{N_s}\sum_{i=1}^{N_s}\sum_{j=1}^{N}(x_j^i - \overline{x}_j)^2 / \sum_{j=1}^{N}(x_j^{\text{true}})^2, \quad (28)$$

$$\text{MSE} = \text{Bias}^2 + \text{Var}, \quad (29)$$

where $\bar{x}$ is the ensemble mean of the image estimates and N_s is the total number of noisy realizations ($N_s = 10$ in this simulation). Furthermore, we computed the contrast recovery coefficient (CRC) of the blood pool and tumor. The CRC is calculated by

$$\text{CRC}_i = \frac{1}{N_s}\sum_{i=1}^{N_s}|\overline{S}_i - \overline{B}_i| / \overline{B}_i \quad (30)$$

where $\bar{S}_i$ denotes the mean activity of the region of interest and $\bar{B}_i$ denotes the mean activity of the white matter region (background) in the ith reconstructed image.

Figure 4 shows the true image of time frame 2 and reconstructed image samples by different methods. This frame has a scan duration of 20 seconds and a total of 26k events (very low counts). For each method, the reconstructed image is shown with the minimum MSE, which was minimized by varying either the iteration number in the EM-based methods or the regularization parameter β in the regularization-based methods. The results of a high-count frame (frame 24, 727k events) are shown in Fig. 5. Fig. 6 compares the ensemble mean

squared bias versus ensemble variance tradeoff achieved by different reconstruction methods by varying either the iteration number or the regularization parameter in each method for frame 2 and frame 24. We can see that by using the kernel matrix obtained from the composite images, the kernelized EM (KEM) substantially improved the image quality over the conventional ML-EM for both the low-count and high-count frames. For the very low count frame, the KEM also achieved substantially less bias at a fixed variance than any other method in the study. In Fig. 7(a) we plot the minimum MSE achieved by different methods for all time frames. The error bars represents plus and minus one standard deviation, which was estimated by bootstrapping the 10 noisy realizations. The corresponding scan duration and count level of each frame are given in Fig. 7(b). In general, the proposed kernel method achieved the lowest MSE for nearly all frames and substantially outperformed all other methods for low-count frames.

Figure 8 compares the contrast recovery coefficient (CRC) versus background noise trade-off achieved by different methods for two regions of interest (ROI). The blood pool was the ROI in frame 2 and the tumor was the ROI in frame 24. The white matter region was chosen as background to calculate the noise standard deviation (SD). Again, the plots showed that the proposed method achieved a higher CRC with a lower background noise than other methods, especially for the low-count frame.

D. Effect of Kernel Parameters

Fig. 9(a) shows the image MSE values of different frames as functions of k, the number of nearest neighbors in the kernel method. The image MSE generally decreases as the k value becomes larger because more pixels are correlated in the kernel matrix to reduce noise. However, an overly large k may lead to an increase in MSE if the image contains some objects that are of small size but high target-to-background contrast, such as the image of frame 2 in Fig. 4. This is because correlating the pixels in these high-contrast small objects to pixels in other flat regions can result in many small weights in the kernel matrix which in turn lead to underestimation of the high contrast object. A large k also results in a dense $\boldsymbol{K}$ matrix and higher computation cost for reconstruction. Overall, the kernelized reconstruction achieved a relatively stable MSE with a value of k between 20 and 100 for the two selected frames.

The radial Gaussian was found to be generally better than the polynomial kernel in terms of MSE in our simulations. Here we focus on investigating the σ parameter in the Gaussian kernel. Fig. 9(b) shows the effect of σ on MSE. A small σ can differentiate feature points more easily, but is less effective to suppress noise. As σ grows larger, kernels become smoother and significant noise reduction is achieved. When σ becomes too large, the kernel value by the radial Gaussian function approaches 1 and the resulting MSE also remains constant. Since the features points $\{f_j\}$ are normalized, we found that σ value between 0.1 and 10 provides good results.

E. Reconstruction of a Small Target

Reconstruction of a small target in the presence of background activity can be a challenge in PET imaging, as small targets may either be visually obstructed by noise in an unregularized

reconstruction or be over-smoothed by regularization. The latter occurs in KEM if the *k* number in *k*NN is far greater than the size of a small target. Many false neighbors may be included in the *k*NN search, which in turn will over-smooth the small target. To address this problem, we can modify the *k*NN strategy in Eq. (21) by thresholding the nonzero weights in the kernel matrix by a threshold τ to remove false neighbors. We validated this modified strategy using a new stimulation study with a smaller brain tumor (6 mm in diameter) (Fig. 10(a)). All the other settings in the simulation remained the same. Since most weighting factors in the kernel matrix by *k*NN are between 0.9 and 1.0, we set the threshold τ to 0.96 in the modified strategy.

We compare the reconstructed images by the MLEM, EM-NLM and proposed KEM in Fig. 10. All reconstruction methods were run for 100 iterations. The MLEM image has a tumor CRC of 0.70 but with a high background noise SD=28.4%. The post-smoothed image by NLM reduces noise but also decreases the contrast (CRC=0.54). In comparison, the KEM preserves the tumor contrast (CRC=0.67) while reducing noise in the background by more than a factor of 2 (SD=12.6%). A more complete comparison of the tumor CRC versus background noise SD using 10 realizations is shown in Fig. 11(a). A temporal-smoothing method, EM-PCA, is also included. The curves are plotted by varying the iteration number in each method. The KEM demonstrates a more robust performance of CRC versus noise than other methods. Fig. 11(b) shows the CRC vs. SD plots for the blood pool region in frame 2. Clearly, the improvement achieved by the proposed KEM is much more pronounced for the low-count frame. These results demonstrate that the *k*NN with thresholding for constructing kernel matrix can work robustly for reconstruction of both large and small targets.

F. Incomplete Composite Image Prior

The kernel method works best when the structures in each frame are all embedded in the composite images. If a region cannot be identified in the composite images, the reconstruction accuracy of the region may suffer. To address this potential problem, we can combine the *k*NN approach defined in Eq. (21) with the local window approach in Eq. (23) to avoid introducing long-range correlations. An application example of the local *k*NN in MR-guided PET image reconstruction is reported in [51]. Here we applied the method to dynamic PET reconstruction.

Fig. 12 shows the reconstructed images of frame 2 by the KEM and EM-NLM using either the complete composite images (all three composite frames in Fig. 2) or the middle 20-minute frame only (incomplete prior case). In both cases, the kernel matrix was constructed using the local *k*NN approach that selects 20 nearest neighbors from each 9×9 neighborhood. Although it shows that the local *k*NN results in a slightly higher MSE for both the KEM and EM-NLM methods than the global *k*NN results in Fig. 4, the modified KEM, when using the complete composite images, still outperforms all other reconstructions shown in Fig. 4. When the kernel matrix was constructed using only the middle 20-minute composite image, the boundary of the blood pool become blurrier in reconstructed images. Nonetheless, the KEM still achieved lower MSE than the EM-NLM that uses the same

kernel matrix, and other reconstructions shown in Fig. 4 that do not use the composite image.

IV. Application to Dynamic PET Patient Scan

We have applied the proposed kernel method to a dynamic PET scan of a real patient. The data set was acquired using a GE Discovery PET/CT 690 scanner with the patient in the prone position. The PET scan started right at the injection and lasted 60 minutes. The dynamic PET data were divided into 18 time frames: 3×20 s, 3×40 s, 3×60 s, 3×180 s, 3×300 s, 3×600 s. A CT scan was acquired to provide the attenuation map for attenuation correction. Attenuation factors, detector efficiencies and dead time correction factors were incorporated in the forward model. Randoms and scatters were estimated using the manufacturer software and were modeled as an additive background.

To derive the composite image prior, the 60-minute dynamic data were rebinned into three 20-minute frames. Each rebinned frame was reconstructed using the OSEM with 30 subsets and 2 iterations. The kernel matrix was then derived using the same procedure as described in Section III-B. For each voxel, k=50 nearest neighbors in a $7 \times 7 \times 7$-voxel local region were used. The use of the local window is to reduce the computation time. The σ value of the radial Gaussian kernel function was set to 1. The original 18 time frames of the dynamic PET scan were then reconstructed individually by the kernelized EM algorithm with 100 iterations.

The kernelized reconstruction was compared with the traditional EM reconstruction that contains no prior and the EM followed by a NLM post-filtering that uses the same kernel matrix. In our previous simulation, the EM-NLM method was found to outperform other existing methods. Fig. 13 shows the 3D reconstructions of two different time frames by the three methods at iteration 50. Frame 3 has a 20-second scan duration and frame 18 has a 10-minute scan duration. The reconstructed images by MLEM have good contrast in the blood pool and myocardium regions (indicated by "A" and "B" respectively) but contain high noise in uniform regions. By using the composite image prior, the EM-NLM reduces noise but at the expense of reducing contrast of the blood and myocardium. In comparison, the kernelized EM not only smooths out noise in uniform regions but also preserves the boundary and intensity of the blood and myocardium very well.

Quantitative comparisons are shown in Fig. 14. The mean values of two regions of interest (blood pool and myocardium in frame 3 and frame 18, respectively) are plotted as functions of background noise standard deviation by varying the iteration number of each method from 20 to 100. A uniform region inside the liver was chosen as the background and the standard deviation (SD) of the voxel intensity values in the region was calculated. The results show that at the same ROI mean value, the kernelized EM reconstruction always has a lower background noise than the MLEM. The NLM post-filtering removed noise as effectively as the kernelized EM does, but the intensities in the regions of interest were substantially reduced.

V. Conclusion

In this paper, we propose a kernel method to model PET image intensity as a function of feature points obtained from prior knowledge. The kernelized image model can incorporate prior information in the forward projection model. The maximum likelihood estimate can be easily obtained using the popular EM algorithm. Dynamic PET simulation results show that the proposed reconstruction method can achieve better performance than the conventional ML-EM reconstruction and TV regularization, and also outperforms the ML-EM with post filtering (e.g. EM-HYPR and EM-NLM), other prior-image-based regularization methods (the Bowsher method and PICCS) and temporal-smoothing methods (EM-PCA and KL-PWLS) for low-count frames. The proposed kernelized EM algorithm has been applied to reconstruct the dynamic PET images of a breast cancer patient and has achieved promising results.

The kernel method is suitable for applications where prior images can be obtained to represent accurately the spatial structures of the image to be reconstructed. Such cases include dynamic PET, dynamic contrast-enhanced CT and MRI, as well as static image reconstruction with a matched anatomical prior. We note that the kernel method mainly explores the spatial correlations embedded in data and can be combined with temporal smoothing techniques (e.g. direct reconstruction methods [50]) to obtain more improvement on dynamic image reconstruction. One thing that needs further study is the framing of composite frames which can be chosen to provide optimized composite image priors for specific applications. In addition, patient motion, if not corrected, may result in mismatches between the composite images and the dynamic images to be reconstructed, which will affect performance of the kernel method. Therefore, incorporation of motion compensation in the kernel method will be part of our future investigations.

Acknowledgments

References

1. Qi J, Leahy RM. Iterative reconstruction techniques in emission computed tomography. Physics in Medicine and Biology. 2006; 51(15):R541–R578. [PubMed: 16861768]

2. Bai B, Li Q, Leahy RM. Magnetic resonance-guided positron emission tomography image reconstruction. Seminars in Nuclear Medicine. 2013; 43(1):30–44. [PubMed: 23178087]

3. Leahy R, Yan X. Incorporation of anatomical MR data for improved functional imaging with PET. Information Processing in Medical Imaging. 1991; (511):105–120. Lecture Notes in Computer Science.

4. Fessler JA, Clinthorne NH, Rogers WL. Regularized emission image reconstruction using imperfect side information. IEEE Transactions on Nuclear Science. 1992; 39(5):1464–1471.

5. Gindi G, Lee M, Rangarajan A, Zubal IG. Bayesian reconstruction of functional images using anatomical information as priors. IEEE Transactions on Medical Imaging. 1993; 12(4):670–680. [PubMed: 18218461]

6. Ouyang X, Wong WH, Johnson VE, Hu X, Chen CT. Incorporation of correlated structural images in PET image reconstruction. IEEE Transactions on Medical Imaging. 1994; 13(4):627–640. [PubMed: 18218541]

7. Bowsher JE, Johnson VE, Turkington TG, Jaszczak RJ, Floyd CE, Coleman RE. Bayesian reconstruction and use of anatomical a priori information for emission tomography. IEEE Transactions on Medical Imaging. 1996; 15(5):673–686. [PubMed: 18215949]

8. Lipinski B, Herzog H, Rota Kops E, Oberschelp W, Mller-Grtner HW. Expectation maximization reconstruction of positron emission tomography images using anatomical magnetic resonance information. IEEE Transactions on Medical Imaging. 1997; 16(2):129–36. [PubMed: 9101322]

9. Bowsher JE, Yuan Hong, Hedlund LW, Turkington TG, Akabani G, Badea A, Kurylo WC, Wheeler CT, Cofer GP, Dewhirst MW, Johnson GA. Utilizing MRI information to estimate F18-FDG distributions in rat flank tumors. 2004 IEEE Nuclear Science Symposium Conference Record. 2004; 4:2488–2492.

10. Somayajula S, Panagiotou C, Rangarajan A, Li Q, Arridge SR, Leahy RM. PET image reconstruction using information theoretic anatomical priors. IEEE Transactions on Medical Imaging. 2011; 30(3):537–49. [PubMed: 20851790]

11. Tang J, Rahmim A. Bayesian PET image reconstruction incorporating anato-functional joint entropy. Physics in Medicine and Biology. 2009; 54(23):7063. [PubMed: 19904028]

12. Chan C, Fulton R, Feng DD, Meikle S. Regularized image reconstruction with an anatomically adaptive prior for positron emission tomography. Physics in Medicine and Biology. 2009; 54(24): 7379–400. [PubMed: 19934490]

13. Cheng-Liao J, Qi J. PET image reconstruction with anatomical edge guided level set prior. Physics in Medicine and Biology. 2011; 56(21):6899. [PubMed: 21983558]

14. Bousse, A.; Pedemonte, S.; Kazantsev, D.; Ourselin, S.; Arridge, S.; Hutton, BF. Weighted MRI-Based Bowsher Priors for SPECT Brain Image Reconstruction. Conference Record of Nuclear Science Symposium Conference Record (NSS/MIC); 2010; IEEE; 2010. p. 3519-3522.

15. Kazantsev D, Bousse A, Pedemonte S, Arridge SR, Hutton BF, Ourselin S. Edge preserving bowsher prior with nonlocal weighting for 3D SPECT reconstruction. 2011 IEEE International Symposium on Biomedical Imaging (ISBI). 2011:1158–1161.

16. Vunckx K, Atre A, Baete K, Reilhac A, Deroose CM, Van Laere K, Nuyts J. Evaluation of three MRI-based anatomical priors for quantitative PET brain imaging. IEEE Transactions on Medical Imaging. 2012; 31(3):599–612. [PubMed: 22049363]

17. Gilboa G, Osher S. Nonlocal linear image regularization and supervised segmentation. SIAM Multiscale Modeling and Simulation. 2007; 6(2):595–630.

18. Nguyen, VG.; Lee, SJ. Nonlocal-means approaches to anatomy-based PET image reconstruction. Conference Record of Nuclear Science Symposium Conference Record (NSS/MIC); 2010; IEEE; 2010. p. 3273-3277.

19. Nguyen VG, Lee SJ. Incorporating anatomical side information into PET reconstruction using nonlocal regularization. IEEE Transactions on Image Processing. Oct; 2013 22(10):3961–3973. [PubMed: 23744678]

20. Chun, SY.; Fessler, JA.; Dewaraja, YK. Non-local means methods using CT side information for I-131 SPECT image reconstruction. Conference Record of Nuclear Science Symposium Conference Record (NSS/MIC); 2012; IEEE; 2012. p. 3362-3366.

21. Chen GH, Tang J, Leng S. Prior image constrained compressed sensing (PICCS): A method to accurately reconstruct dynamic CT images from highly undersampled projection data sets. Medical Physics. 2008; 35(2):660–663. [PubMed: 18383687]

22. Chen GH, Tang J, Hsieh JJ. Temporal resolution improvement using PICCS in MDCT cardiac imaging. Medical Physics. 2009; 36(6):2130–5. [PubMed: 19610302]

23. Lubner MG, Pickhardt PJ, Tang J, Chen GH. Reduced image noise at low-dose multidetector CT of the abdomen with prior image constrained compressed sensing algorithm. Radiology. 2011; 260(1):248–56. [PubMed: 21436086]

24. Wang, GB.; Catana, C.; Qi, J. Joint reconstruction of attenuation and emission from PET data using MR-derived attenuation prior. IEEE Nuclear Science Symposium and Medical Imaging Conference (NSS-MIC 12); Anaheim, California, USA. November 2012; (abstract only)

25. Mistretta CA, Wieben O, Velikina J, Block W, Perry J, Wu Y, Johnson K, Wu Y. Highly constrained backprojection for time-resolved MRI. Magnetic Resonance in Medicine. 2006; 55(1): 30–40. [PubMed: 16342275]

26. O'Halloran RL, Wen Z, Holmes JH, Fain SB. Iterative projection reconstruction of time-resolved images using highly-constrained back-projection (HYPR). Magnetic Resonance in Medicine. 2008; 59(1):132–9. [PubMed: 18058939]

27. Christian BT, Vandehey NT, Floberg JM, Mistretta CA. Dynamic PET denoising with HYPR processing. Journal of Nuclear Medicine. 2010; 51(7):1147–54. [PubMed: 20554743]

28. Hofmann T, Scholkopf B, Smola AJ. Kernel methods in machine learning. The Annals of Statistics. 2008; 36(3):1171–1220.

29. Friedman JH, Bentely J, Finkel RA. An algorithm for finding best matches in logarithmic expected time. ACM Transactions on Mathematical Software. 1977; 3(3):209–226.

30. Buades A, Coll B, Morel JM. On image denoising methods. SIAM Multiscale Modeling and Simulation. 2005; 4(2):490–530.

31. Chan, C.; Meikle, S.; Fulton, R.; Tian, GJ.; Cai, W.; Feng, DD. A nonlocal post-filtering algorithm for PET incorporating anatomical knowledge. Conference Record of Nuclear Science Symposium Conference Record (NSS/MIC); 2009; IEEE; 2009. p. 2728-2732.

32. Kazantsev D, Arridge SR, Pedemonte S, Bousse A, Erlandsson AK, Hutton BF, Ourselin S. An anatomically driven anisotropic diffusion filtering method for 3D SPECT reconstruction. Physics in Medicine and Biology. 2012; 57(12):3793–810. [PubMed: 22617131]

33. Shepp LA, Vardi Y. Maximum likelihood reconstruction in positron emission tomography. IEEE Transactions on Medical Imaging. 1982; MI-1:113–122. [PubMed: 18238264]

34. Lange K, Carson RE. EM reconstruction algorithms for emission and transmission tomography. Journal of Computer Assisted Tomography. 1984; 8(2):306–316. [PubMed: 6608535]

35. Hudson HM, Larkin RS. Accelerated image reconstruction using ordered subsets of projection data. IEEE Transactions on Medical Imaging. 1994; 13(4):601–609. [PubMed: 18218538]

36. Wang, GB.; Qi, J. PET image reconstruction using kernel method. IEEE International Symposium on Biomedical Imaging (ISBI); San Francisco, CA. April 2013; p. 1162-1165.

37. Zhou, Y.; Wang, Y.; Ying, L. A kernel-based compressed sensing approach to dynamic MRI from highly undersampled data. IEEE International Symposium on Biomedical Imaging (ISBI); San Francisco, CA. April 2013; p. 310-313.

38. Qi, H.; Hughes, S. Using the kernel trick in compressive sensing: accurate signal recovery from fewer measurements. IEEE International Conference on Acoustics, Speech, and Signal Processing (ICASSP); May 2011; p. 3940-3943.

39. Wang G, Qi J. Acceleration of the direct reconstruction of linear parametric images using nested algorithms. Physics in Medicine and Biology. 2010; 55(5):1505–1517. [PubMed: 20157226]

40. Rudin LI, Osher S, Fatemi E. Nonlinear total variation based noise removal algorithms. Phys D: Nonl Phen. 1992; 60:259–268.

41. De Pierro AR. A modified expectation maximization algorithm for penalized likelihood estimation in emission tomography. IEEE Transactions on Medical Imaging. 1995; 14(1):132–137. [PubMed: 18215817]

42. King MA, Miller T. Use of nonstationary temporal Wiener filter in nuclear medicine. European Journal of Nuclear Medicine. 1985; 10(9–10):458–461. [PubMed: 4006989]

43. Yap JT, Treffert JD, Chen CT, Cooper MD. Image processing of dynamic images with principal components analysis. Radiology. 1992; 185:177.

44. Huang, CC.; Yu, X.; Bading, J. Feature extraction by subspace fitting of time activity curve in PET dynamic studies. IEEE Nuclear Science Composium and Medical Imaging Conference; 1997. p. 1721-1735.

45. Kao CM, Yap JT, Mukherjee J, Wenick MN. Image Reconstruction for Dynamic PET Based on Low-Order Approximation and Restoration of the Sinogram. IEEE Transactions on Medical Imaging. 1997; 16(6):738–749. [PubMed: 9533575]

46. Wernick MN, Infusino EJ, Milosevic M. Fast spatiotemporal image reconstruction for dynamic PET. IEEE Transactions on Medical Imaging. 1999; 18(3):185–95. [PubMed: 10363697]

47. Li Q, Asma E, Sangtae A, Leahy RM. A fast fully 4-D incremental gradient reconstruction algorithm for list mode PET data. IEEE Transactions on Medical Imaging. 2007; 26(1):58–67. [PubMed: 17243584]

48. Rahmim A, Tang J, Zaidi H. Four-dimensional image reconstruction strategies in dynamic PET: Beyond conventional independent frame reconstruction. Medical Physics. 2009; 36(8):3654–3670. [PubMed: 19746799]

49. Tsoumpas C, Turkheimer FE, Thielemans K. A survey of approaches for direct parametric image reconstruction in emission tomography. Medical Physics. 2008; 35(9):3963–3971. [PubMed: 18841847]

50. Wang GB, Qi J. Direct estimation of kinetic parametric images for dynamic PET. Theranostics. 2013; 3(10):802–815. [PubMed: 24396500]

51. Hutchcroft W, Wang GB, Qi J. Anatomical-image aided PET reconstruction by the kernel method. Journal of Nuclear Medicine. 2014; 55(supplement 1) Abstract No. 44.

52. Harrison, RL.; Vannoy, SD.; Haynor, DR., et al. Preliminary Experience with the Photon History Generator Module of a Public-Domain Simulation System for Emission Tomography. Conference Record of IEEE Nuclear Science Symposium and Medical Imaging Conference; 1993. p. 1154-1158.

(a)   (b)
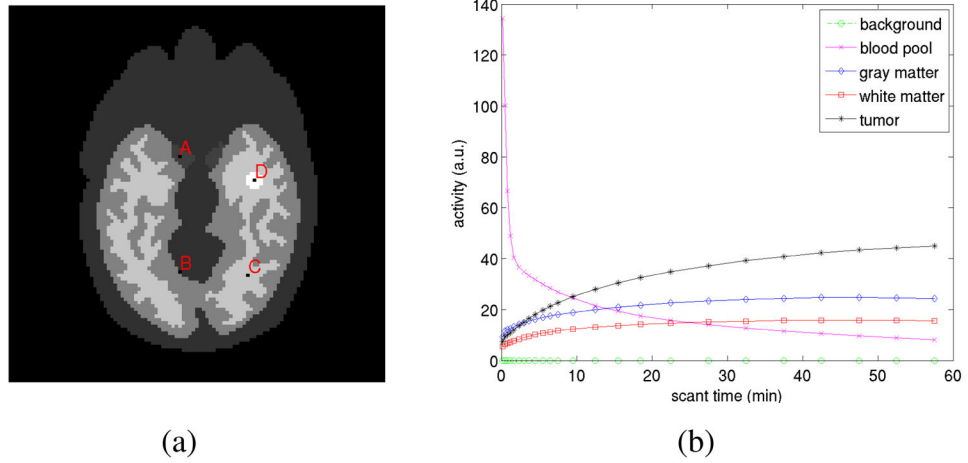
Fig. 1.
The digital phantom and time activity curves used in the simulation studies. (a) The Zubal brain phantom composed of gray matter, white matter and a tumor (15mm in diameter); (b) the regional time activity curves.

(a) first 20 minutes   (b) middle 20 minutes
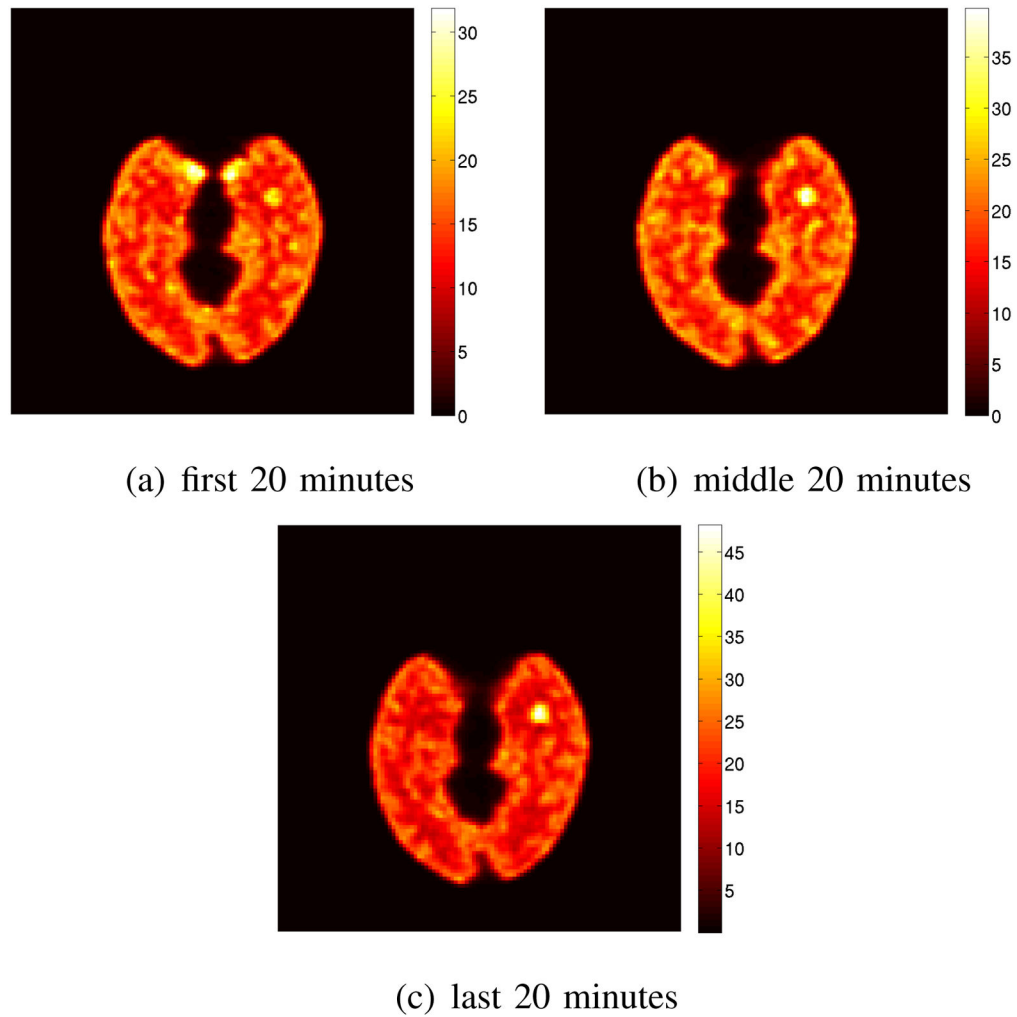
(c) last 20 minutes

Fig. 2.
Composite images reconstructed from the rebinned dynamic sinograms: (a) the first 20 minutes, (b) the middle 20 minutes, and (c) the last 20 minutes.

(a) pixel A

(b) pixel B

(c) pixel C

(d) pixel D
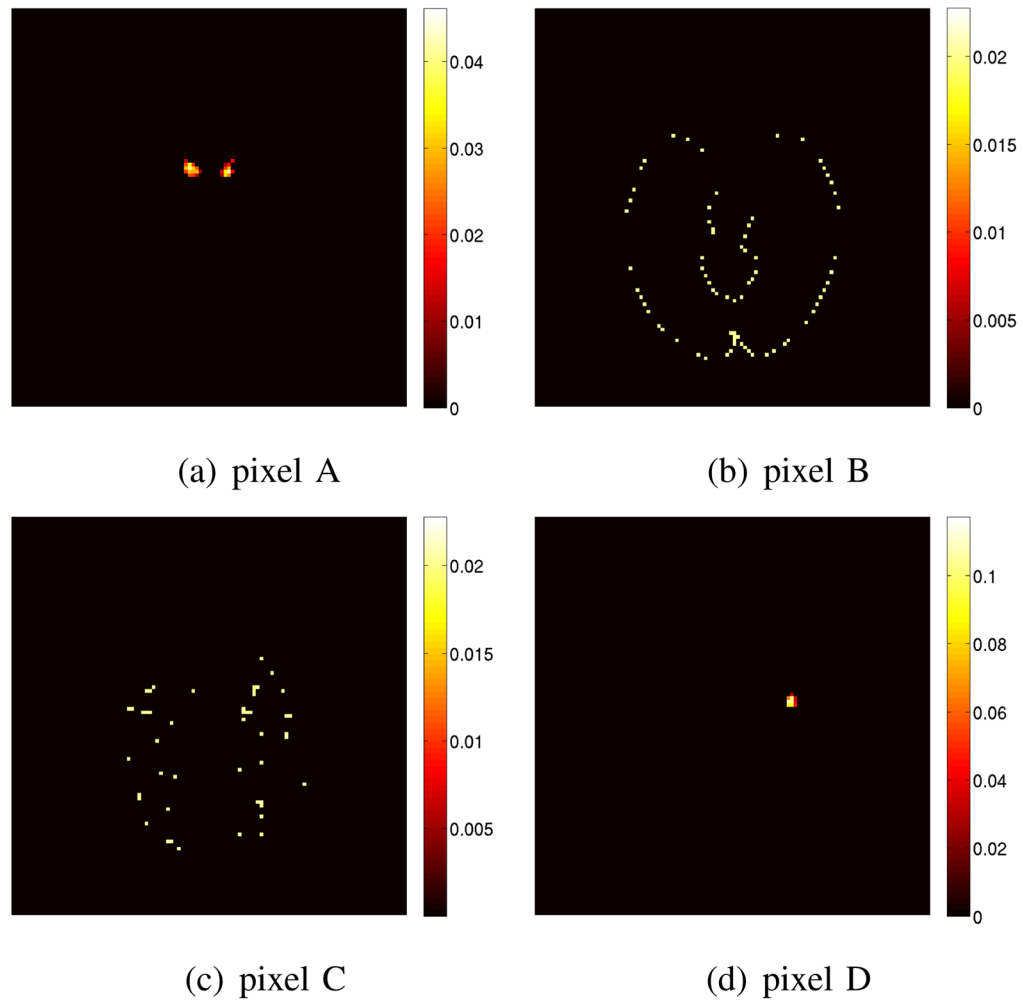
Fig. 3.
Basis images reshaped from four different columns of the kernel matrix $\bar{\boldsymbol{K}}$ derived from the composite images shown in Fig. 2. The four chosen pixels are located in the blood region, at the gray matter edge, in the white matter and in the tumor region and marked by "A", "B", "C" and "D" in Fig. 1(a), respectively.
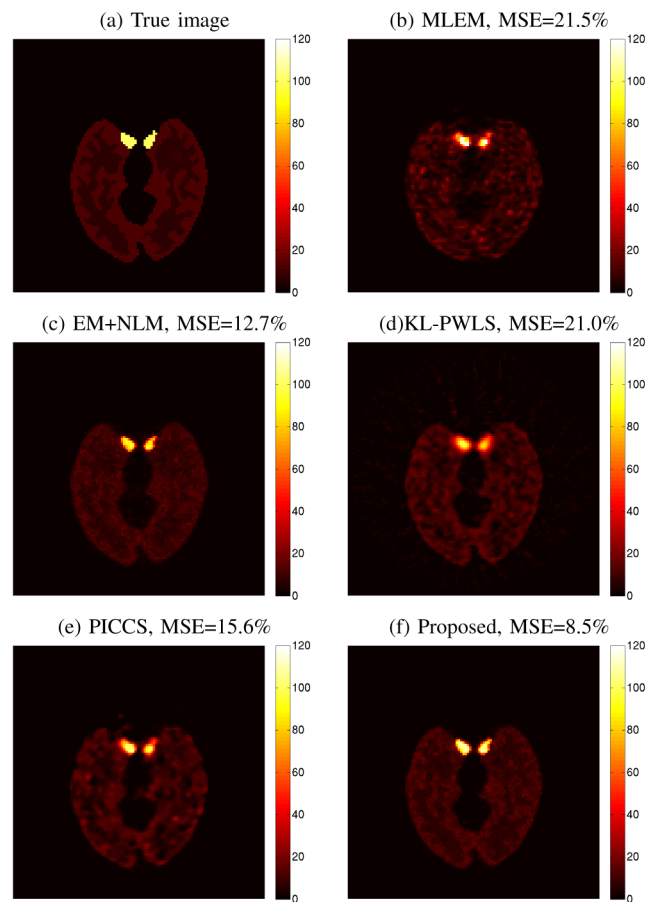
Fig. 4.
The true activity image (a) and reconstructed images (b)–(f) by different methods for frame 2 (scan duration: 20s; counts: 26k). (b) ML-EM reconstruction, (c) EM followed by NLM denoising, (d) KL-PWLS, (e) PICCS, and (f) the proposed kernelized reconstruction.
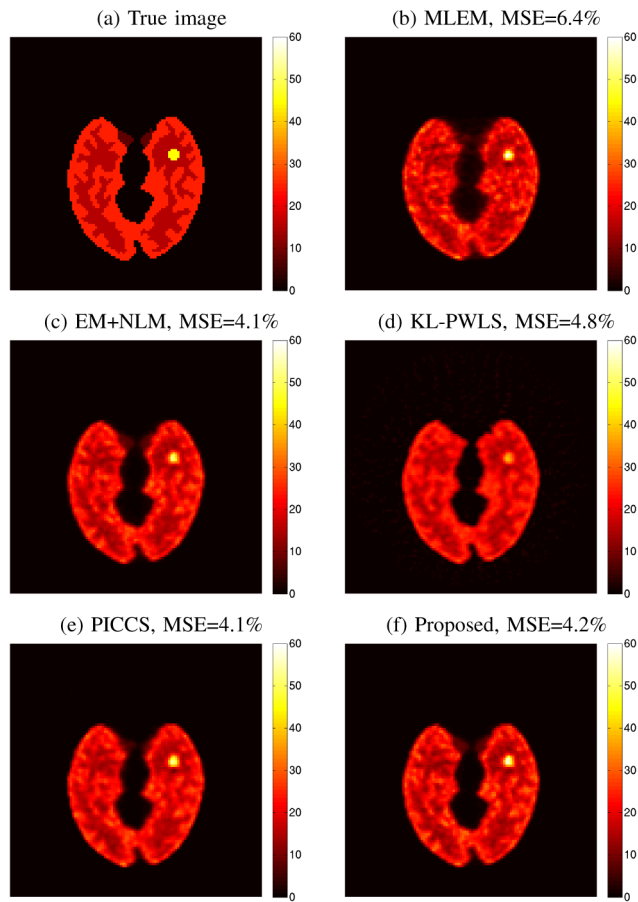
Fig. 5.
The true activity image (a) and reconstructed images (b)–(h) by different methods for frame 24 (scan duration: 300s; counts: 727k). (b) ML-EM reconstruction, (c) EM followed by NLM denoising, (d) KL-PWLS, (e) PICCS, and (f) the proposed kernelized reconstruction.
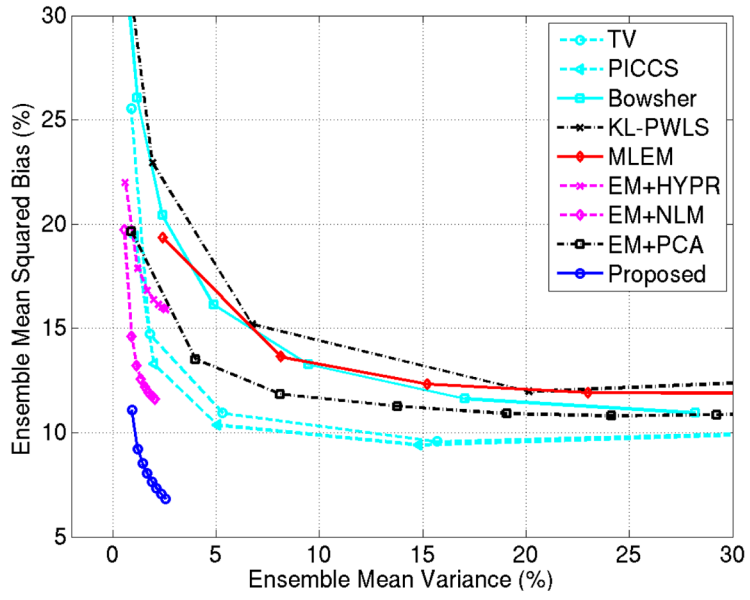
(a) frame 2
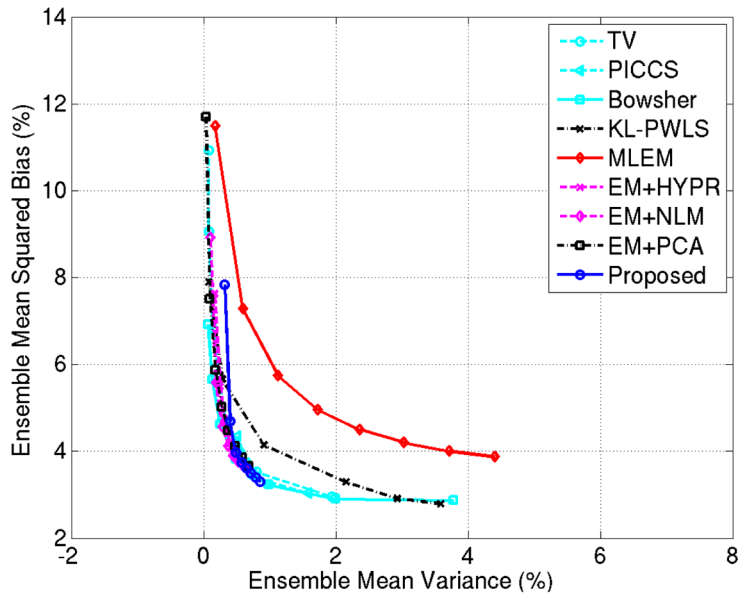
(b) frame 24

Fig. 6.
Ensemble mean squared bias versus mean variance trade-off achieved by different reconstruction methods in (a) frame 2, 26k counts, and (b) frame 24, 727k counts.
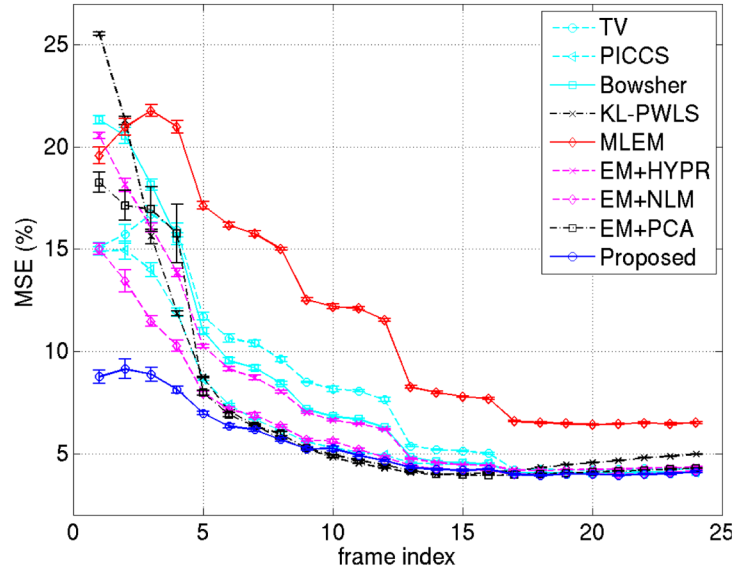
(a) minimum MSE
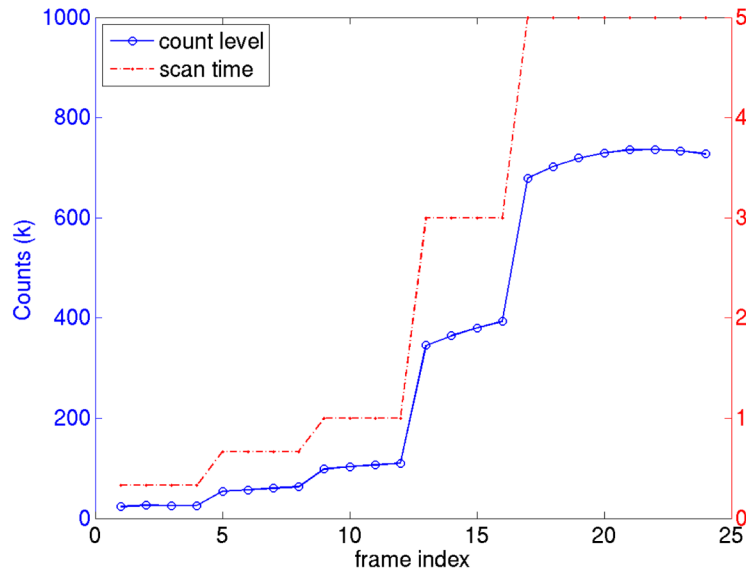
(b) counts and scan time

Fig. 7.
(a) Comparisons of the minimum MSE for all frames achieved by different reconstruction methods. The tuning variable is iteration number for EM-based methods and β for regularization-based methods. (b) The total number of counts and scan duration of each time frame.
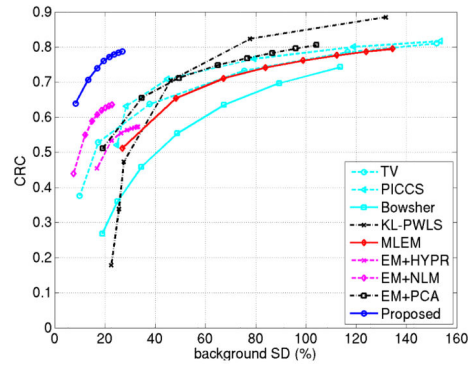
(a) blood pool
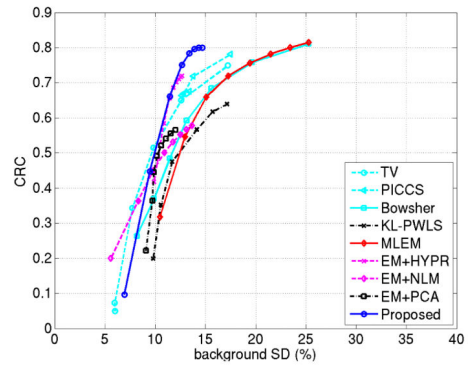
(b) tumor

Fig. 8.

Contrast recovery coefficient (CRC) of regions of interest versus background noise. (a) blood pool region in frame 2, (b) tumor region in frame 24.
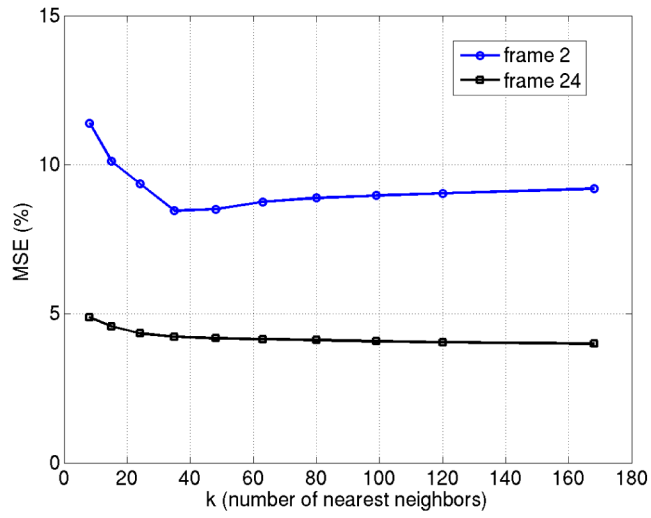
(a) Effect of k (b) Effect of σ
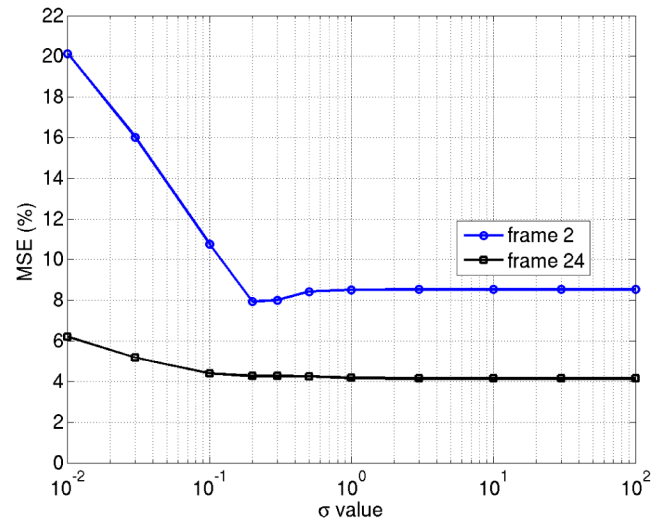
Fig. 9.
Effect of kernel parameters (a) k and (b) σ on image MSE.
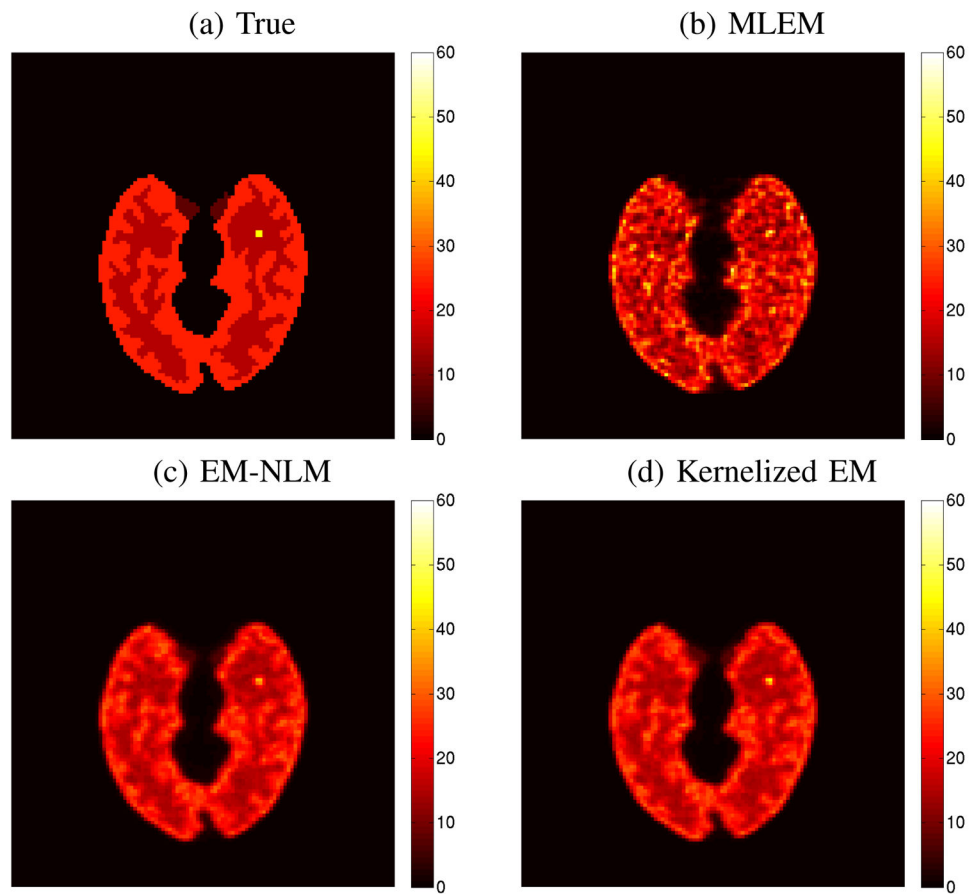
Fig. 10.
The true activity image (a) and reconstructed images (b)-(d) for the last frame of a brain phantom that is similar to the one defined in Fig. 1 but with a smaller tumor (6mm in diameter). (a) true image of the last frame, (b) ML-EM reconstruction (tumor CRC=0.70, background SD=28.4%), (c) EM followed by NLM denoising (CRC =0.54, SD = 12.1%), and (d) proposed kernelized EM (CRC=0.67, SD=12.6%). All reconstructions were run for 100 iterations.
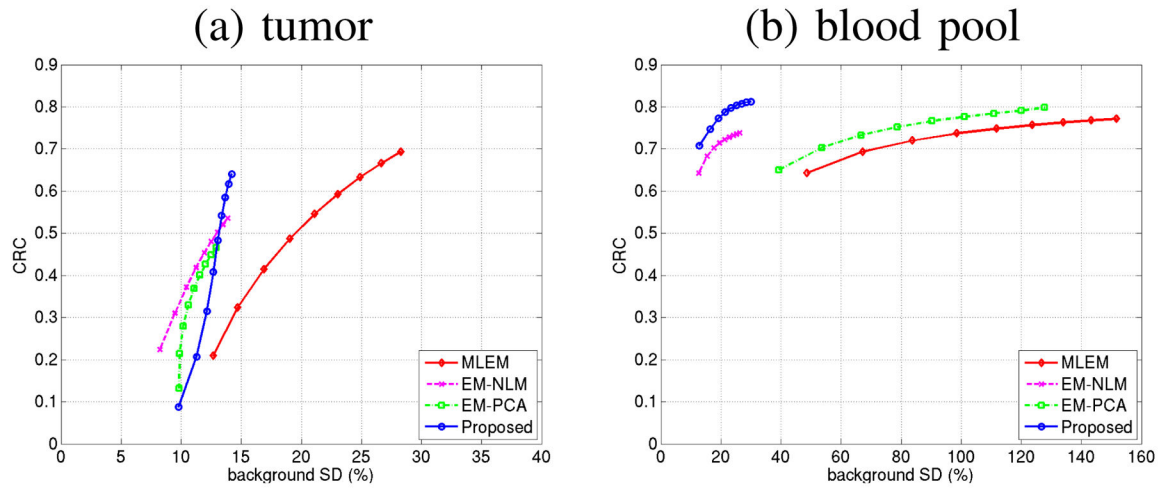
Fig. 11.
Plots of contrast recovery coefficient (CRC) of regions of interest versus noise SD in background with varying the iteration number from 20 to 100. (a) tumor in the last frame, (b) blood pool in frame 2.
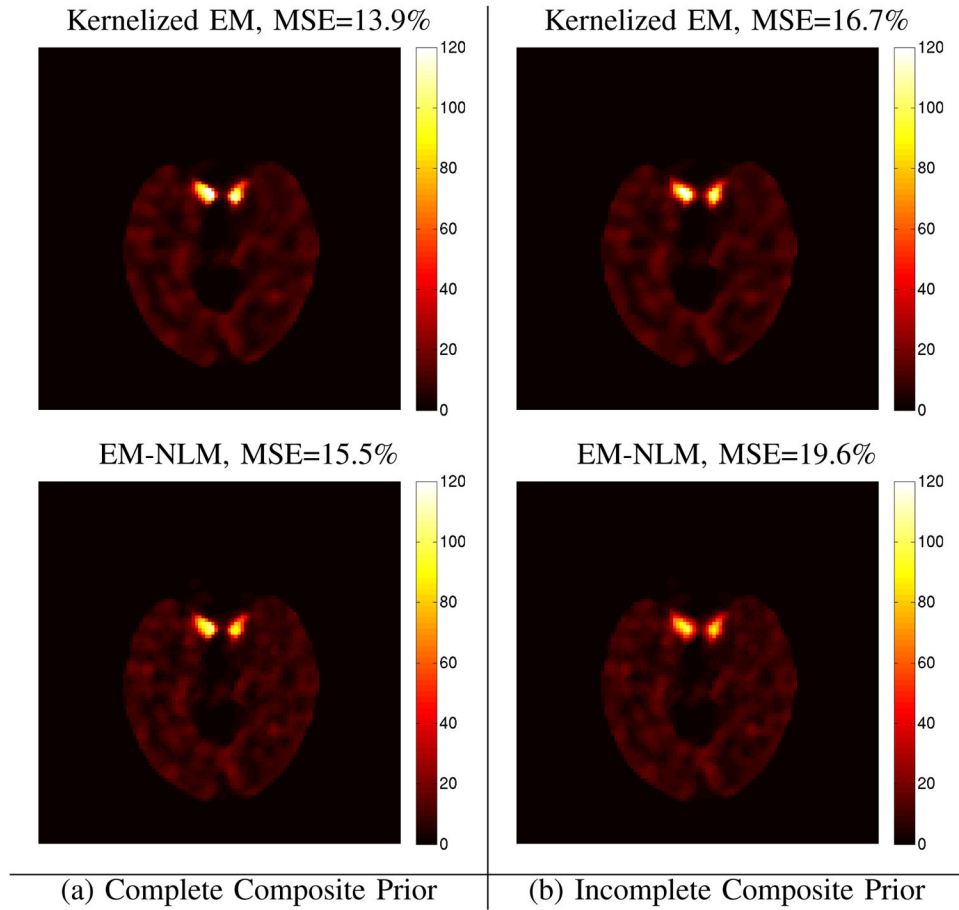
Fig. 12.
Reconstructed images of frame 2 by the EM-NLM and proposed KEM using local *k*NN. The kernel matrix was constructed using a local neighborhood with (a) the complete (all three) composite images in Fig. 2, and (b) only the middle 20-minute composite frame in Fig. 2.
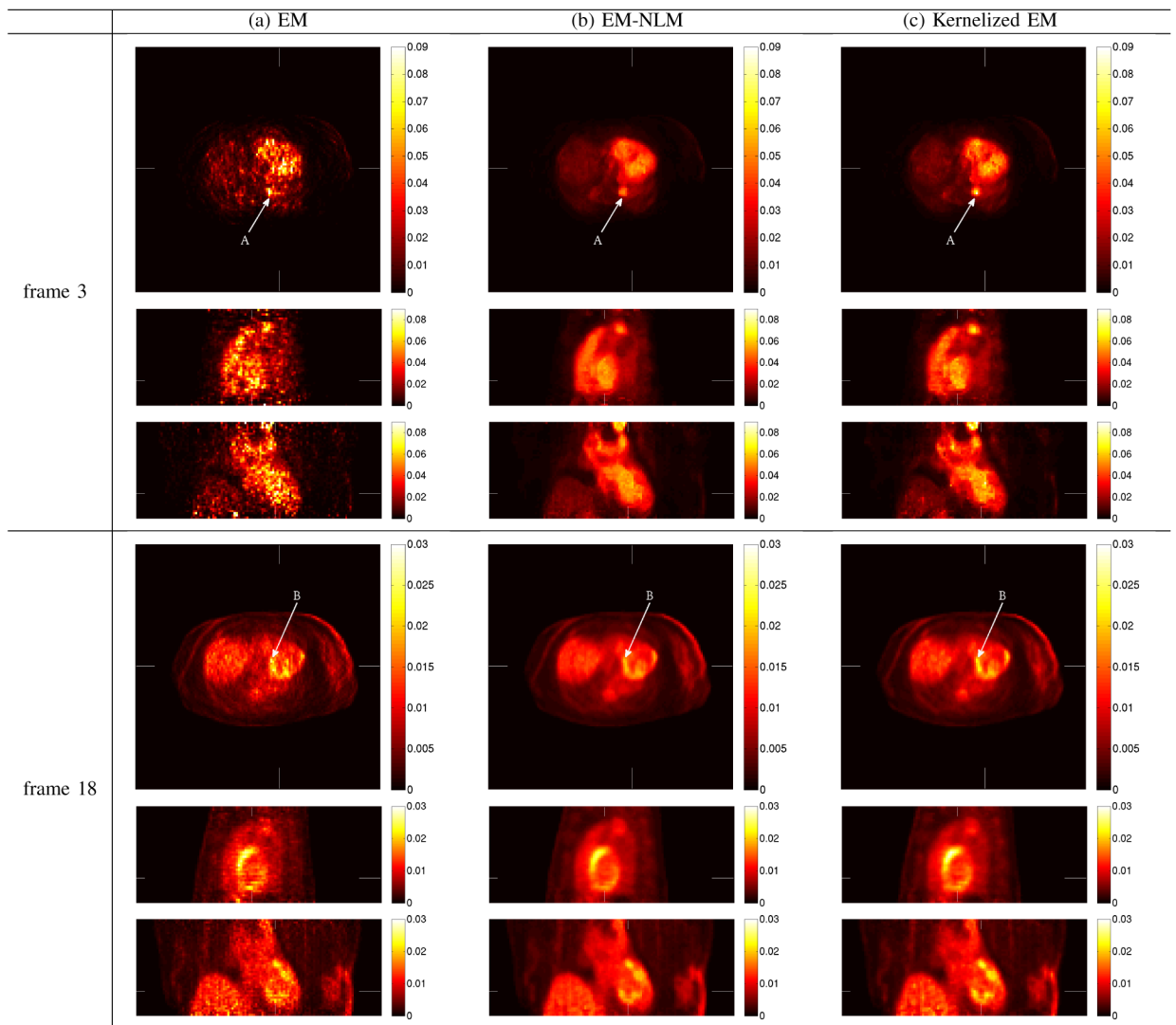
Fig. 13.
Reconstructed images of a short early frame (#3) and a long late frame (#18) of the real patient data by different algorithms with 50 iterations. (a) MLEM, (b) EM followed by NLM, and (c) proposed kernelized EM reconstruction. Each 3D reconstruction is shown in transverse, sagittal and coronal views.
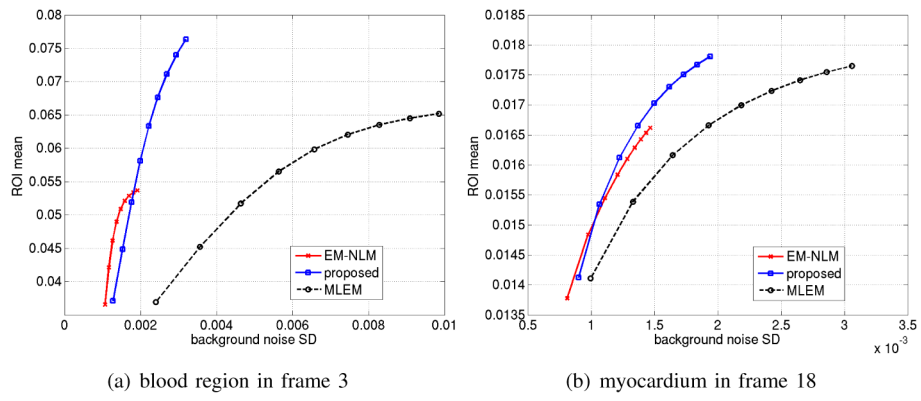
(a) blood region in frame 3

(b) myocardium in frame 18

Fig. 14.
Plots of ROI mean of (a) the blood region and (b) myocardium versus liver background
noise by varying iteration number from 20 to 100 with an increment of 10.